Journal of Materials Chemistry A

ROYAL SOCIETY OF CHEMISTRY

COMMUNICATION

Cite this: *J. Mater. Chem. A*, 2020, **8**, 19799

Received 30th July 2020
Accepted 21st September 2020

DOI: 10.1039/d0ta07457h

rsc.li/materials-a

A chemically stable cucurbit[6]uril-based hydrogen-bonded organic framework for potential SO_2/CO_2 separation†

Jun Liang,[ab] Shanghua Xing,[ab] Philipp Brandt,[b] Alexander Nuhnen,[b] Carsten Schlüsener,[b] Yangyang Sun[b] and Christoph Janiak[*ab]

A cucurbit[6]uril cage-based hydrogen-bonded organic framework (HOF) shows high capacity of SO_2 capture (up to 4.98 mmol g^{-1} at 1 bar and 293 K), high SO_2/CO_2 selectivity, good chemical stability toward dry SO_2, and outstanding cycling performance. The preferential adsorption sites on the cage of the HOF are revealed by DFT calculations and FT-IR.

The release of toxic gas pollutants such as sulphur dioxide (SO_2) into the atmosphere is a worldwide risk of growing concern.[1,2] Anthropogenic SO_2 emissions are mainly caused by the combustion of fossil fuels with high sulphur content causing serious detriment on the environment (*i.e.* smog and acid rain) and risk for human health.[3,4] In addition, SO_2 is noxious to many industrial operations, such as degrading the performance of adsorbents for CO_2 removal from flue-gas,[5] and deactivating the catalysts in CH_4 combustion and NO_x reduction.[6] Currently, flue gas desulfurization (FGD) can be performed by limestone scrubbing and ammonia scrubbing techniques to remove only about 90–99% SO_2 from the gas mixtures.[7] Thus, the development of porous solid adsorbents for the selective removal of the remaining SO_2 from flue gas and other SO_2-containing gases is warranted for a sustainable development.[1]

Along this direction, an increasing number of porous materials, including zeolites,[8] metal–organic frameworks (MOFs),[9–14] and covalent organic frameworks (COFs),[15,16] have been evaluated to give promising results due to their high Brunauer–Emmett–Teller (BET) surface areas, high pore volume and programmed structures. Besides, amorphous materials, such as poly(ionic liquid)s,[17] have also attracted attention for their high uptake capacity and high stability. Porous organic cage (POC) based crystalline materials are a newly developed class of porous materials, in which the pores consist of the intrinsic pores in the cage itself and the potential extrinsic pores from the POC molecule packing in the crystal structure.[18–20] POCs have aroused great interest during the last decade for their unique features, such as defined structures based on strong covalent bonds, tuneable intrinsic and extrinsic pores for specific guest molecules and, good solubility in certain solvents for easy subsequent processing.[21–24] The rapid development of POC-based materials including hydrogen-bonded organic frameworks (HOFs) has led to promising applications including gas capture and storage,[25] vapor sorption,[26] molecular separations,[27] and pollutant removal.[28] However, POC-based crystalline materials are barely investigated for toxic gas capture and separation, such as SO_2 separation from SO_2-containing gas mixtures.[29,30]

Cucurbit[6]uril (CB6 or Q6), synthesized by the condensation of formaldehyde and glycoluril under acidic conditions, has a hydrophobic cavity with a diameter of 5.8 Å and two symmetric hydrophilic windows with a pore diameter of about 3.9 Å.[31] The unique properties of CB6 cage have led to various applications from catalysis to molecular sorption and separation due to its excellent chemical and thermal stability reported by Kim *et al.*[32,33] In the hydrogen-bonded organic framework of CB6–H (H stands for polymorph H)[34] (Fig. 1), the windows of each CB6 molecule are partially blocked by adjacent CB6 cages by the formed hydrogen bonds. Yet, polar molecules like CO_2 could enter the intrinsic pores of CB6 thanks to the dynamic HOF architecture. Herein, we have investigated the properties of this very stable HOF CB6–H with honeycomb-like structures and channel-type pores with a diameter of 6 Å for SO_2 storage and separation.

To achieve the maximum accessibility and gas uptake of CB6 molecules in the HOF, a short diffusion path length seemed desirable and nanoCB6–H particles were prepared with sizes between 100 nm and 500 nm based on scanning electron microscopy (SEM) and transmission electron microscopy (TEM) analyses (Fig. S1, ESI†). The phase purity of nanoCB6–H is confirmed by powder X-ray diffraction (PXRD) (Fig. 2a). In

[a]*Hoffmann Institute of Advanced Materials, Shenzhen Polytechnic, Liuxian Blvd, Nanshan District, Shenzhen 7098, China. E-mail: janiak@uni-duesseldorf.de*

[b]*Institut für Anorganische Chemie und Strukturchemie, Heinrich-Heine-Universität Düsseldorf, Universitätsstraße 1, Düsseldorf 40225, Germany*

† Electronic supplementary information (ESI) available: Synthesis, structures, SEM image, TGA, PXRD, isotherms and tables. See DOI: 10.1039/d0ta07457h

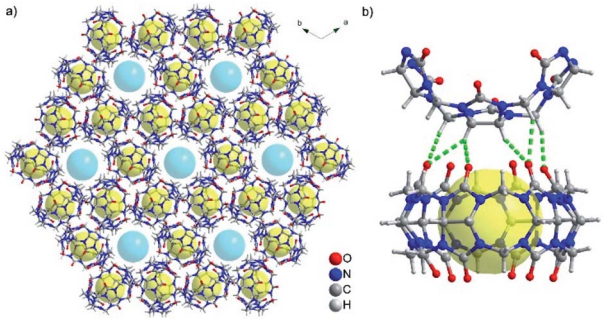

Fig. 1 (a) View of the honeycomb-like hydrogen-bonded organic framework of CB6–H along the *c*-axis. All solvent molecules are omitted. (b) The intermolecular C–H···O hydrogen bonds (2.24 to 2.60 Å) between neighbouring CB6 molecules in CB6–H. The yellow sphere represents the intrinsic pore while the blue sphere represents the extrinsic pores with a diameter of 6 Å (CCDC no. 676880, Refcode KOBNEV).

addition, nanoCB6–H can be stable up to 300 °C in air as suggested by the temperature-dependent PXRD and TGA curves (Fig. S2 and S3, ESI†). NanoCB6–H features a BET surface area of 441 $m^2 g^{-1}$ and a total pore volume of 0.22 $cm^3 g^{-1}$ before SO_2 sorption (Fig. 2b and Table S1, ESI†). Pore size distribution (PSD) analysis indicates the existence of dominant micro tunnels at 6 Å and hierarchical defect mesopores (2–5 nm) (Fig. S4, ESI†).

As a first exposure to dry SO_2 resulted in a slight drop in SO_2 uptake capacity, after which the values remained constant (Fig. 3b), all porosity values discussed hereafter refer to a 'recycled' sample which had been exposed to dry SO_2 in order to have reproducible uptake results. Recycled nanoCB6–H shows high SO_2 uptake capacity (120 $cm^3 g^{-1}$ at 293 K and 0.97 bar), good chemical stability towards dry SO_2, excellent recyclability over ten successive runs and high IAST selectivity of 120 for SO_2/CO_2 (molar ratio 10/90) gas mixtures at 1 bar. The strong interactions between CB6 and SO_2 molecules are revealed by experimental sorption results and DFT calculations. The results obtained indicate that nanoCB6–H is promising for SO_2 gas separations under application-oriented conditions.

NanoCB6–H recycled *e.g.* over 7th run exhibits type-I isotherms for SO_2 with high uptakes of 120 $cm^3 g^{-1}$ (corresponding to 4.98 mmol g^{-1}) and 140 $cm^3 g^{-1}$ (corresponding to 6.18 mmol g^{-1}) at 293 K and 273 K at 0.97 bar, respectively (Fig. 2c and S5, ESI†). Using the total pore volume, the storage density of SO_2 in nanoCB6–H is calculated to be 1.52 g cm^{-3} at 293 K, which is 57% of the liquid density of SO_2 (2.63 g cm^{-3}) at 263 K indicating the efficient packing of SO_2 in the pores of nanoCB6–H. To the best of our knowledge, these are the highest uptake values for organic cage-based materials in the literature

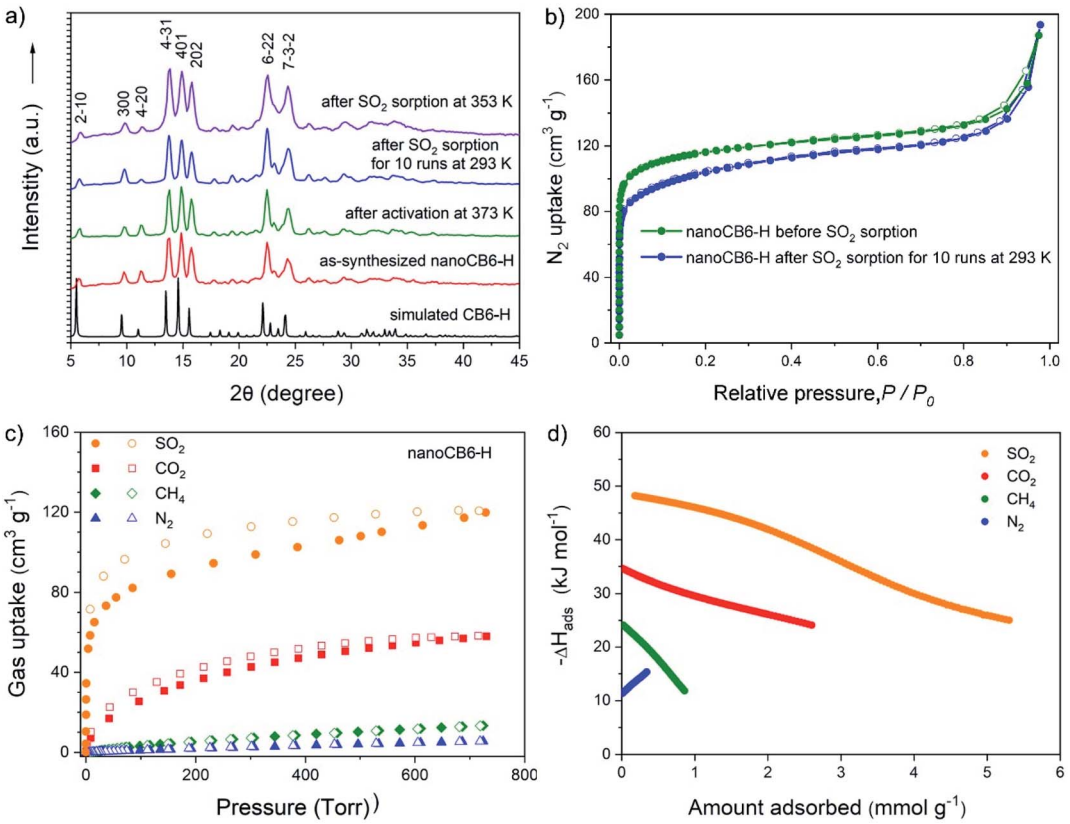

Fig. 2 (a) PXRD data and (b) nitrogen-sorption isotherms at 77 K of nanoCB6–H materials before and after SO_2 sorption. (c) Single gas sorption isotherms measured for recycled nanoCB6–H at 293 K. Filled and empty symbols refer to adsorption and desorption, respectively. (d) Isosteric enthalpy of adsorption of SO_2, CO_2, CH_4, and N_2 for recycled nanoCB6–H materials. 'Recycled' refers to a sample measured after first exposure to dry SO_2.

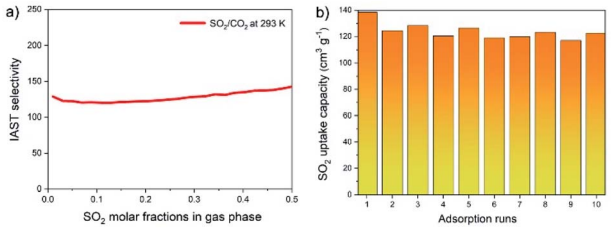

Fig. 3 (a) IAST selectivities of SO_2/CO_2 mixtures with varying SO_2 molar fractions in gas phase at 293 K and 1 bar. (b) Successive SO_2 adsorption capacity in recycles of nanoCB6–H at 293 K and 0.97 bar.

so far (Table S5, ESI†). It should be noted that the SO_2 adsorption isotherms of nanoCB6–H exhibit a steep increase in the low relative pressure range and the SO_2 uptake reaches 81 cm^3 g^{-1} at 0.1 bar. These values also outperform other porous materials with similar BET surface areas, such as MFI zeolite (61.1, 68.5),[35] MOFs including ELM-12 (43.7, 61.2),[36] KAUST-8 (39.7, 70.3),[37] SIFSIX-3-Zn (46.2, 51.3),[38] Prussian blue analogues ZnCo (13.3, 44),[39] and FMOF-2 (10.8, 43.7)[40] at both 0.1 bar and 1 bar, respectively (Fig. S6, S7 and Table S6, ESI†). Furthermore, the desorption branch of SO_2 sorption shows a hysteresis from 0.97 bar to 0.01 bar, indicating relatively strong SO_2 interaction with nanoCB6–H. We expect this CB6-based HOF to display a highly selective SO_2 uptake capability in gas desulfurization processes due to the existence of polar carbonyl and C–H groups in the ring.

As expected, recycled nanoCB6–H shows good CO_2 uptake capacities with 58 cm^3 g^{-1} at 0.97 bar and 293 K, which is higher than the reported value (45 cm^3 g^{-1}) (Fig. 2c and S8, ESI†).[34] It is worth noting that, although CO_2 has a smaller kinetic diameter (3.30 Å) than SO_2 (4.1 Å), the CO_2 uptake was much lower than SO_2 (120 cm^3 g^{-1}). In addition, the SO_2 adsorption isotherm is obviously steeper than the CO_2 adsorption isotherm, indicating stronger affinity toward SO_2 by nanoCB6–H. This is supported by its much higher isosteric enthalpy of adsorption at zero loading, ΔH^0_{ads} of −48 kJ mol^{-1} for SO_2 compared to −35 kJ mol^{-1} for CO_2 (Fig. 2d). These results suggest that the interactions between CB6 molecules with polar groups and SO_2 molecules are much stronger than those with CO_2, which might be explained by the higher polarizability of SO_2 (47.7×10^{-25} cm^3) than that of CO_2 (29.1×10^{-25} cm^3) and a higher dipole moment of SO_2 (1.62 D) than that of CO_2 (0 D).[37] In contrast, nanoCB6–H only displays a small CH_4 and N_2 uptake with 13.3 and 5.5 cm^3 g^{-1} under 0.97 bar at 293 K, respectively (Fig. 2c, S9 and S10, ESI†). This can be explained by the low polarizability for CH_4 (5.88×10^{-50} cm^3) and N_2 (17.4×10^{-25} cm^3). The much steeper increase of SO_2 adsorption isotherms than for CO_2 *etc.* at low pressures indicates a high application potential of nanoCB6–H in FGD processes, where residual SO_2 (up to 500 ppm) needs to be removed.

To evaluate the potential of nanoCB6–H for separating SO_2 from binary gas mixtures, we applied ideal adsorbed solution theory (IAST) calculations on dual-site Langmuir (DSLAI) fitted isotherms to determine selectivities of mixed-gas adsorption with the "3P sim" software.[41] The best fits for our isotherms were achieved with the DSLAI fitting model with fitting parameters given in Table S3.† IAST calculations have been widely used in predicting gas separation performance and proved to be a first and reliable estimation of the selectivity within low pressure range.[42] The results from the IAST calculations indicate that recycled nanoCB6–H holds IAST selectivities between 120 and 142 for SO_2/CO_2 gas mixtures with the molar ratio between 1/99 and 50/50 at 293 K and 1 bar (Fig. 3a and S15–S18†). To best of our knowledge, the SO_2/CO_2 IAST selectivity value obtained with nanoCB6–H is the highest among reported cage-based materials and even comparable to the leading MOFs in the literature (Fig. S19 and Table S6, ESI†). Moreover, the IAST selectivities are 662 for SO_2/CH_4, and 1720 for SO_2/N_2 with a molar ratio of 10 : 90 gas mixtures at 293 K and 1 bar (Fig. S20, S21 and Table S4, ESI†).

In addition to the excellent selectivity, the recycle capability of nanoCB6–H is also very important for evaluating the application potential. Thus, we have conducted ten successive runs of SO_2 adsorption at 293 K on nanoCB6–H. It is observed the SO_2 uptake capacity decreases only slightly from 138 cm^3 g^{-1} to 124 cm^3 g^{-1} for the first and the second run, respectively, and an uptake around 120 cm^3 g^{-1} can be readily reached for the next runs (Fig. 3b and S22, ESI†). This shows that after an initial loss of uptake capacity, SO_2 is ad- and desorbed to the same degree in the following cycles. The ΔH^0_{ads} values also decrease from −65 kJ mol^{-1} for newly activated to −48 kJ mol^{-1} for recycled nanoCB6–H samples (Fig. S23, ESI†), indicating that some strong binding sites for SO_2 are lost during the first run. $\Delta H^0_{ads} = -48$ kJ mol^{-1} for SO_2 in this HOF is similar to those reported for some MOFs, and indicates a regeneration of this material under relatively mild conditions (Table S6, ESI†). The PXRD analyses indicate that nanoCB6–H could retain its crystallinity after SO_2 sorption for ten runs (Fig. 2a). The decreased SO_2 uptake capacity is accompanied by a slightly decreased BET surface areas from 441 to 383 m^2 g^{-1} and decreased micropore volumes after ten runs (Fig. 2b and Table S1, ESI†), which might be caused partially by the detrimental effect of very small amount of "sulfurous acid" species formed by SO_2 and residual water molecules in nanoCB6–H (Fig. S25†). In general, nanoCB6–H shows excellent recycle stability in SO_2 adsorption experiments at 293 K up to 0.97 bar.

We further evaluated the sorption properties of nanoCB6–H at 353 K, which is a common temperature to condense water vapor before flue gas desulfurization.[12] As expected, the gas uptake capacities at 353 K and 0.97 bar for SO_2 and CO_2 decreased to 66 and 9.6 cm^3 g^{-1}, respectively (Fig. S26, ESI†). Still, the SO_2 adsorption curve remains of type I, and shows a steep rise up to 20 cm^3 g^{-1} at 0.01 bar, and quickly approaches 63% (42 cm^3 g^{-1} at 0.1 bar) of the maximum uptake (66 cm^3 g^{-1} at 0.97 bar). Notably, the desorption branch of SO_2 sorption still shows a hysteresis from 0.97 bar to 0.01 bar, indicating strong SO_2 interaction with nanoCB6–H at 353 K. In contrast, CO_2 is poorly adsorbed by nanoCB6–H at this temperature (Fig. S26, ESI†). As a result, SO_2/CO_2 selectivities remain high because of the low CO_2 affinities at 353 K, thereby positioning nanoCB6–H as the first HOF ever reported for SO_2 removal and separation which we see as a subsequent benchmark system. The

structural stability of nanoCB6–H is demonstrated by the PXRD analyses (Fig. 2a).

Encouraged by the strong SO_2 affinity and high SO_2/CO_2 selectivity based on IAST predictions, we simulated breakthrough curves with a gas mixture of $N_2/CO_2/SO_2$ (84.9 : 15 : 0.1 v/v/v) at 293 K based on the DSLAI-fitted isotherm data of nanoCB6–H (Table S3, ESI†). Our previous work on SO_2 separation showed that breakthrough simulations can give a good and reliable estimate for the breakthrough onset time of SO_2 in microporous MOFs.[12] The simulated breakthrough plot in Fig. S27† shows an immediate rise of the N_2 and CO_2 concentrations at the outlet, indicating the relatively low sorption capacity for N_2 and CO_2 of nanoCB6–H under the set conditions. In contrast, SO_2 could be retained for about 760 min g^{-1} in nanoCB6–H, which indicates its solid separation capability for SO_2 *versus* CO_2 at 293 K and 1 bar.

To better understand the results of the SO_2 sorption with nanoCB6–H at 293 K, we revisited the HOF structure, elemental analysis and TGA results. To estimate the accessible cavity void of CB6–H, the solvent molecules were eliminated to give a cavity volume of 2671 $Å^3$ per unit cell (Fig. S28, ESI†). As the molecular volumes of SO_2 are accessible from its solid-state structures ($V_{SO_2} = 55$ $Å^3$),[43] the theoretical amount of SO_2 per unit cell of nanoCB6–H was calculated to be about 48 molecules. On the other hand, the uptake capacity of 4.98 mmol g^{-1} of SO_2 by nanoCB6–H at 293 K indicates the activated nanoCB6–H adsorbs ~45 molecules per unit cell, which is close to the theoretical value (48). The observed slightly lower amount of adsorbed SO_2 molecules in nanoCB6–H can probably be ascribed to the presence of trace water in HOF nanoparticles. While the higher amount of adsorbed SO_2 with a value of 55 molecules per unit cell by nanoCB6–H at 273 K was due to weaker adsorbed SO_2 molecules on the external surfaces. This is also evident from the difference in ΔH_{ads} values ranging from −48 kJ mol^{-1} for the stronger binding sites until −25 kJ mol^{-1} for the weaker external interactions.

In order to gain a molecular understanding of the exceptional good adsorption performance of nanoCB6–H, we used DFT-D3 (dispersion-corrected DFT) calculations to investigate the possible binding sites for SO_2 by CB6 cages. Gas-phase geometry optimization of SO_2 with CB6 yields five different possibilities (SO_2^{I}, SO_2^{II}, SO_2^{III}, SO_2^{IV}, and SO_2^{V}) for SO_2 binding (Fig. 4 and Table S7, ESI†). Specifically, SO_2 can be located above the portal plane (SO_2^{I}), in the portal plane (SO_2^{II}), and in the cavity of CB6 cage (SO_2^{III}). SO_2 molecules are mainly adsorbed through the $S^{\delta+}\cdots O^{\delta-}$ electrostatic interaction with the O=C group of CB6 with a S···O distance of 2.69–3.04 Å, indicating an extremely strong interaction that arises from the positive charge of the S atom in the SO_2 molecule and the electronegative nature of the carbonyl group with binding energies up to −82 kJ mol^{-1} (site III, Table S7, ESI†). It should be noted that the intrinsic pore of CB6 is large enough to encapsulate two SO_2 molecules, which have intermolecular $S^{\delta+}\cdots O^{\delta-}$ interactions (3.40 Å) in the confined space (Fig. 4 and S29, ESI†). Moreover, SO_2 can be located around the outer surface to form binding sites (SO_2^{IV} and SO_2^{V}), which involve multiple $S^{\delta+}\cdots O^{\delta-}$ and $S^{\delta+}\cdots N^{\delta-}$ electrostatic interactions (2.63 Å and 3.52 Å,

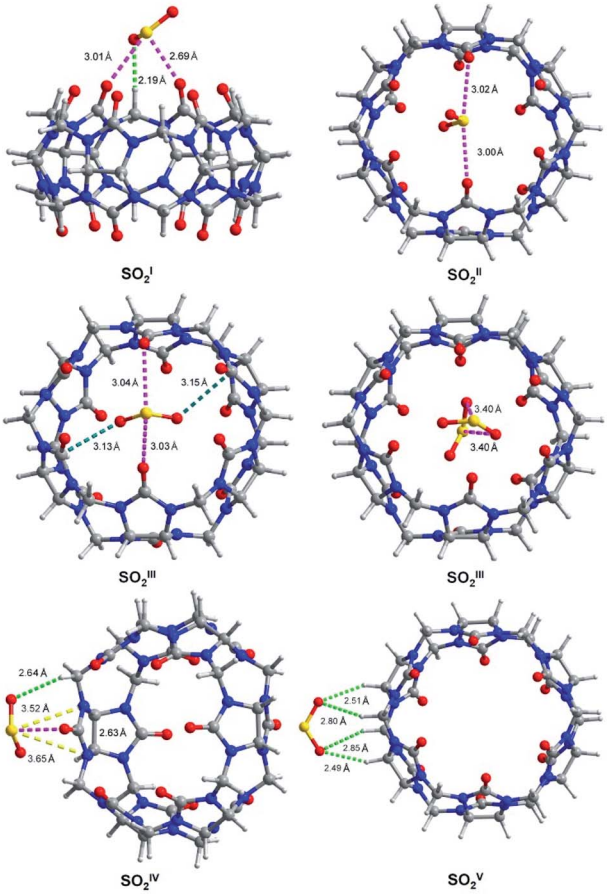

Fig. 4 View of the binding sites of SO_2 molecules with the CB6 cage as determined by DFT calculations. The closest contacts between SO_2 molecules and CB6 cages are depicted by dashed lines: $O_2S\cdots O{=}C$ in pink; $SO_2\cdots H{-}C$ in light green; $SO_2\cdots C{=}O$ in teal; $O_2S\cdots N$ in yellow.

respectively), and $O^{\delta-}\cdots H^{\delta+}$ dipole–dipole interactions between O atoms of SO_2 molecules and C–H atoms of CB6 cages with a $O^{\delta-}\cdots H^{\delta+}$ distance of 2.49–2.85 Å. Considering the structural features of nanoCB6–H (Fig. 1), in which each portal of CB6 is partially blocked by an adjacent cage, SO_2^{III}, SO_2^{IV}, and SO_2^{V} are suggested to be the predominant binding sites, while SO_2^{I}, SO_2^{II} could be available in defect areas and on the external surfaces of nanoCB6–H. DFT calculated static binding energies of SO_2 molecules on CB6 are −82, −50, and −19 kJ mol^{-1} for SO_2^{III}, SO_2^{IV}, and SO_2^{V}, confirming the strong interaction between SO_2 molecules and nanoCB6–H. The higher static SO_2 binding energies (−82 kJ mol^{-1}) than the experimental ΔH_{ads} value (−48 kJ mol^{-1}) is caused by the limitation of the DFT approach. Thus, SO_2 molecules could be firmly trapped around or in CB6 cages *via* the $S^{\delta+}\cdots O^{\delta-}$ and $O^{\delta-}\cdots H^{\delta+}$ interactions.

To verify the interactions predicted by DFT calculations above, FT-IR spectroscopic studies of nanoCB6–H loaded with dry SO_2 under atmosphere conditions show a new peak at 1144 cm^{-1} assigned to the symmetric stretch of adsorbed SO_2, which is redshifted from 1152 cm^{-1} ($\Delta = -8$ cm^{-1}) for free SO_2,[11] demonstrating its interaction with CB6 cages (Fig. S30, ESI†). The V_3 asymmetric stretch bands of SO_2 (between

1361 cm^{-1} and 1320 cm^{-1}) are not observed due to overlap with the strong vibration bands of nanoCB6–H. Moreover, significant vibrational changes in the framework were also observed after SO_2 adsorption. The carbonyl stretching mode at 1736 cm^{-1} is redshifted to 1730 cm^{-1} ($\Delta = -6$ cm^{-1}), while the methylene stretching mode at 1461 cm^{-1} is blue-shifted to 1465 cm^{-1} ($\Delta = 4$ cm^{-1}), confirming the interactions between SO_2 molecules and carbonyl and, methylene groups of CB6 cages. Moreover, these shifts in the CB6 bands and the appearance of the signals of SO_2 are reversible for recycled nanoCB6–H, suggesting the successful full regeneration of materials (Fig. 3b and S31, ESI†).

To investigate the particle size effect of the CB6-based HOF material with both extrinsic micropores (6 Å) and intrinsic ultramicropores (3.9–5.8 Å), we have prepared micro-size crystallites of CB6–H with a BET surface area of 228 m^2 g^{-1} and a particle size of over 10 μm which were tested for SO_2 sorption (Fig. S32†).[44] As shown in Fig. S33,† CB6–H showed a significantly lower SO_2 uptake capacity (98 cm^3 g^{-1}) than that of nanoCB6–H (145 cm^3 g^{-1}) for the first runs at 293 K and 0.97 bar. Although CB6–H also showed a steep adsorption isotherm at low pressure range, the uptake value of SO_2 (43 cm^3 g^{-1}) was only two thirds of that of nanoCB6–H (63 cm^3 g^{-1}) at 0.01 bar. The much higher SO_2 uptake of nanoCB6–H can be ascribed to its higher surface areas and much smaller particle size (Fig. S1†), which facilitated the faster diffusion of SO_2 molecules to those rich binding sites around and in the CB6 cages of nanoCB6–H (Fig. 4). Although nanoCB6–H shows good stability under dry SO_2 adsorption conditions, an exposure of nanoCB6–H to humid HCl will lead to a phase change and loss of extrinsic pores (Fig. S34†). Thus, application conditions should be carefully considered for CB*n*-based HOF materials,[26] and it's desirable to create acid-stable cage-based materials in the future.[18,45]

In summary, we have studied a cucurbit[6]uril cage-based microporous HOF material, nanoCB6–H, for potential SO_2 capture and separations processes. NanoCB6–H has shown high SO_2 uptake capacity of 4.98 mmol g^{-1} at 293 K, and promising IAST selectivity of 120 for SO_2/CO_2 with a molar ratio 10 : 90 gas mixtures at 1 bar. The excellent selectivity arises from the strong interactions between CB6 cages and SO_2 molecules based on experimental results and DFT calculations. Furthermore, nanoCB6–H features excellent structural stability, recyclability, reprocessing, metal free, and easily scalable synthesis, which make nanoCB6–H a promising material for FGD processes. This work indicates the great potential of functional cage-based HOF materials like nanoCB6–H for SO_2 removal and separations.

Conflicts of interest

There are no conflicts to declare.

Acknowledgements

J. L. and S. X. acknowledge support from the Hoffmann Institute of Advanced Materials (HIAM), Shenzhen Polytechnic. J. L. thanks Dr Fa-Lu Hu in HIAM for scientific discussions. We thank Mr Vasily Gvilava at Heinrich-Heine-Universität Düsseldorf for measuring SEM images and Miss Qiao Wu of Prof. Rong Cao's group at the Fujian Institute of Research on the Structure of Matter, Chinese Academy of Sciences.

Notes and references

1 F. Rezaei, A. A. Rownaghi, S. Monjezi, R. P. Lively and C. W. Jones, *Energy Fuels*, 2015, **29**, 5467–5486.
2 D. A. Cooper, *Atmos. Environ.*, 2003, **37**, 3817–3830.
3 E. Barea, C. Montoro and J. A. Navarro, *Chem. Soc. Rev.*, 2014, **43**, 5419–5430.
4 V. E. Fioletov, C. A. McLinden, N. Krotkov, C. Li, J. Joiner, N. Theys, S. Carn and M. D. Moran, *Atmos. Chem. Phys.*, 2016, **16**, 11497–11519.
5 J. Y. Lee, T. C. Keener and Y. J. Yang, *J. Air Waste Manag. Assoc.*, 2009, **59**, 725–732.
6 J. H. Goo, M. F. Irfan, S. D. Kim and S. C. Hong, *Chemosphere*, 2007, **67**, 718–723.
7 R. K. Srivastava and W. Jozewicz, *J. Air Waste Manag. Assoc.*, 2001, **51**, 1676–1688.
8 Y. Liu, T. M. Bisson, H. Yang and Z. Xu, *Fuel Process. Technol.*, 2010, **91**, 1175–1197.
9 D. Britt, D. Tranchemontagne and a. O. M. Yaghi, *Proc. Natl. Acad. Sci. U. S. A.*, 2008, **105**, 11623–11627.
10 E. Martínez-Ahumada, M. L. Díaz-Ramírez, H. A. Lara-García, D. R. Williams, V. Martis, V. Jancik, E. Lima and I. A. Ibarra, *J. Mater. Chem. A*, 2020, **8**, 11515–11520.
11 G. L. Smith, J. E. Eyley, X. Han, X. Zhang, J. Li, N. M. Jacques, H. G. W. Godfrey, S. P. Argent, L. J. McCormick McPherson, S. J. Teat, Y. Cheng, M. D. Frogley, G. Cinque, S. J. Day, C. C. Tang, T. L. Easun, S. Rudic, A. J. Ramirez-Cuesta, S. Yang and M. Schroder, *Nat. Mater.*, 2019, **18**, 1358–1365.
12 P. Brandt, A. Nuhnen, M. Lange, J. Möllmer, O. Weingart and C. Janiak, *ACS Appl. Mater. Interfaces*, 2019, **11**, 17350–17358.
13 K. Tan, S. Zuluaga, H. Wang, P. Canepa, K. Soliman, J. Cure, J. Li, T. Thonhauser and Y. J. Chabal, *Chem. Mater.*, 2017, **29**, 4227–4235.
14 S. Yang, J. Sun, A. J. Ramirez-Cuesta, S. K. Callear, W. I. David, D. P. Anderson, R. Newby, A. J. Blake, J. E. Parker, C. C. Tang and M. Schroder, *Nat. Chem.*, 2012, **4**, 887–894.
15 G. Y. Lee, J. Lee, H. T. Vo, S. Kim, H. Lee and T. Park, *Sci. Rep.*, 2017, **7**, 557.
16 H. Wang, X. Zeng, W. Wang and D. Cao, *Chem. Eng. Sci.*, 2015, **135**, 373–380.
17 L. Xia, Q. Cui, X. Suo, Y. Li, X. Cui, Q. Yang, J. Xu, Y. Yang and H. Xing, *Adv. Funct. Mater.*, 2018, **28**, 1704292.
18 M. A. Little and A. I. Cooper, *Adv. Funct. Mater.*, 2020, 1909842, DOI: 10.1002/adfm.201909842.
19 M. Mastalerz, *Acc. Chem. Res.*, 2018, **51**, 2411–2422.
20 A. G. Slater and A. I. Cooper, *Science*, 2015, **348**, aaa8075.
21 J. Tian, P. K. Thallapally and B. P. McGrail, *CrystEngComm*, 2012, **14**, 1909–1919.
22 Y. Jin, Q. Wang, P. Taynton and W. Zhang, *Acc. Chem. Res.*, 2014, **47**, 1575–1586.

23 G. Zhang and M. Mastalerz, *Chem. Soc. Rev.*, 2014, **43**, 1934–1947.

24 T. Hasell and A. I. Cooper, *Nat. Rev. Mater.*, 2016, **1**, 16053.

25 P. K. Thallapally, B. P. McGrail, S. J. Dalgarno, H. T. Schaef, J. Tian and J. L. Atwood, *Nat. Mater.*, 2008, **7**, 146–150.

26 Y. Huang, R. H. Gao, M. Liu, L. X. Chen, X. L. Ni, X. Xiao, H. Cong, Q. J. Zhu, K. Chen and Z. Tao, *Angew. Chem., Int. Ed.*, 2020, DOI: 10.1002/anie.202002666.

27 N. Song, T. Kakuta, T.-a. Yamagishi, Y.-W. Yang and T. Ogoshi, *Chem*, 2018, **4**, 2029–2053.

28 G. Crini, *Chem. Rev.*, 2014, **114**, 10940–10975.

29 Only few organic cage-based amorphous materials were reported for SO_2 sorption, see ref. 29 and 30. G. Zhu, J.-M. Y. Carrillo, A. Sujan, C. N. Okonkwo, S. Park, B. G. Sumpter, C. W. Jones and R. P. Lively, *J. Mater. Chem. A*, 2018, **6**, 22043–22052.

30 J. Tian, S. Ma, P. K. Thallapally, D. Fowler, B. P. McGrail and J. L. Atwood, *Chem. Commun.*, 2011, **47**, 7626–7628.

31 S. Lim, H. Kim, N. Selvapalam, K.-J. Kim, S. J. Cho, G. Seo and K. Kim, *Angew. Chem.*, 2008, **120**, 3400–3403.

32 K. Kim, *Chem. Soc. Rev.*, 2002, **31**, 96–107.

33 S. J. Barrow, S. Kasera, M. J. Rowland, J. del Barrio and O. A. Scherman, *Chem. Rev.*, 2015, **115**, 12320–12406.

34 H. Kim, Y. Kim, M. Yoon, S. Lim, S. M. Park, G. Seo and K. Kim, *J. Am. Chem. Soc.*, 2010, **132**, 12200–12202.

35 I. Matito-Martos, A. Martin-Calvo, J. J. Gutierrez-Sevillano, M. Haranczyk, M. Doblare, J. B. Parra, C. O. Ania and S. Calero, *Phys. Chem. Chem. Phys.*, 2014, **16**, 19884–19893.

36 Y. Zhang, P. Zhang, W. Yu, J. Zhang, J. Huang, J. Wang, M. Xu, Q. Deng, Z. Zeng and S. Deng, *ACS Appl. Mater. Interfaces*, 2019, **11**, 10680–10688.

37 M. R. Tchalala, P. M. Bhatt, K. N. Chappanda, S. R. Tavares, K. Adil, Y. Belmabkhout, A. Shkurenko, A. Cadiau, N. Heymans, G. De Weireld, G. Maurin, K. N. Salama and M. Eddaoudi, *Nat. Commun.*, 2019, **10**, 1328.

38 X. Cui, Q. Yang, L. Yang, R. Krishna, Z. Zhang, Z. Bao, H. Wu, Q. Ren, W. Zhou, B. Chen and H. Xing, *Adv. Mater.*, 2017, **29**, 1606929.

39 P. K. Thallapally, R. K. Motkuri, C. A. Fernandez, B. P. McGrail and G. S. Behrooz, *Inorg. Chem.*, 2010, **49**, 4909–4915.

40 C. A. Fernandez, P. K. Thallapally, R. K. Motkuri, S. K. Nune, J. C. Sumrak, J. Tian and J. Liu, *Cryst. Growth Des.*, 2010, **10**, 1037–1039.

41 3P Instruments, *3P sim, Version 1.1.0.7, Simulation and Evaluation Tool for mixSorb*, 3P Instruments, 2018.

42 A. Möller, R. Eschrich, C. Reichenbach, J. Guderian, M. Lange and J. Möller, *Adsorption*, 2017, **23**, 197–209.

43 R. Domínguez-González, I. Rojas-León, E. Martínez-Ahumada, D. Martínez-Otero, H. A. Lara-García, J. Balmaseda-Era, I. A. Ibarra, E. G. Percástegui and V. Jancik, *J. Mater. Chem. A*, 2019, **7**, 26812–26817.

44 J. Liang, A. Nuhnen, S. Millan, H. Breitzke, V. Gvilava, G. Buntkowsky and C. Janiak, *Angew. Chem., Int. Ed.*, 2020, **59**, 6068–6073.

45 R. B. Lin, Y. He, P. Li, H. Wang, W. Zhou and B. Chen, *Chem. Soc. Rev.*, 2019, **48**, 1362–1389.